nature catalysis

Article

https://doi.org/10.1038/s41929-022-00865-5

Biomimetic active sites on monolayered metal–organic frameworks for artificial photosynthesis

Received: 29 November 2021

Accepted: 29 September 2022

Published online: 10 November 2022

Check for updates

Guangxu Lan[1,4], Yingjie Fan[1,4], Wenjie Shi[1,2,3,4], Eric You[1], Samuel S. Veroneau[1] & Wenbin Lin[1]

Enzymes have evolved to catalyse challenging chemical transformations with high efficiency and selectivity. Although a number of artificial systems have been developed to recapitulate the catalytic activity of natural enzymes, they are mostly limited to catalysing relatively simple reactions owing to their ability to mimic only the active metal centres of natural enzymes, without incorporating the proximal amino acids or cofactors. Here we report a metal–organic framework-based artificial enzyme (metal–organic–zyme, MOZ) by integrating active metal centres, proximal amino acids and other cofactors into a tunable metal–organic framework monolayer. We design two libraries of MOZs to perform photocatalytic CO_2 reduction and water oxidation reactions. Through tuning the incorporated amino acids in the MOZs, we systematically optimize the activity and selectivity of these libraries. Combining these optimized MOZs into a single system realizes complete artificial photosynthesis in the reaction of $(1+n)\,CO_2 + 2H_2O \rightarrow CH_4 + nCO + (2+n/2)O_2$.

In nature, enzymes rely on active sites composed of precisely arranged metal centres, amino acids and cofactors to efficiently catalyse chemical reactions. The reactivity and selectivity of metalloenzymes, for example, derives from a complex arrangement of metal ions coordinated to amino acid (AA) side chains and prosthetic groups, a secondary coordination sphere of additional proximal AA side chains and cofactors (for example, pigments, NAD(P)H, ATP) (Fig. 1a)[1]. Importantly, the secondary coordination sphere stabilizes transition states and reactive intermediates through non-covalent interactions, while cofactors provide electrons, hydride equivalents and other species to facilitate reactive pathways. Although a number of artificial systems, including metal clusters[2–5], metal and metal oxide nanoparticles[6], supermolecules and polymers[7], and metal–organic frameworks (MOFs)[8–14], have been developed to mimic the catalytic activity and selectivity of enzymes, current designs of artificial enzymes, however, predominately mimic the active metal centres of enzymes without secondary coordination or additional cofactors[15]. Thus, artificial enzyme systems are currently limited to catalysing relatively simple reactions and lack the systematic tunability required to expand their scope. A general method to rationally design artificial enzymes with complex yet tunable active sites is needed to target increasingly challenging and relevant chemical transformations.

Here we report a metal–organic framework-based artificial enzyme (metal–organic–zyme, MOZ) with precise arrangement of metal centres, amino acids and pigments on a single MOF monolayer to generate well-defined and complex active sites (Fig. 1b). Further, the performance of the MOZs was systematically optimized through the following three steps (Fig. 1c): first, diversification and designing MOZ templates inspired by biocatalysts to create a library of MOZs through the incorporation of AAs; second, selection and screening of these

[1]Department of Chemistry, The University of Chicago, Chicago, IL, USA. [2]College of Chemistry and Chemical Engineering, Xiamen University, Xiamen, China. [3]Present address: MOE International Joint Laboratory of Materials Microstructure, Institute for New Energy Materials and Low Carbon Technologies, School of Materials Science and Engineering, Tianjin University of Technology, Tianjin, China. [4]These authors contributed equally: Guangxu Lan, Yingjie Fan, Wenjie Shi. e-mail: wenbinlin@uchicago.edu

MOZs for specific and enhanced activity; third, optimization and elucidating how this activity is enhanced, allowing for the design of artificial ligands with increased functionality. Through these diversification, selection and optimization processes, the optimized **MOZ-4** with pendant urea groups showed highly active and selective photocatalytic CO_2 reduction reaction (CO_2RR) with turnover numbers (TONs) of 24,740 and 10,352 for CO and CH_4, respectively, and a CO_2RR selectivity of 98.0%, representing a 27-fold increase in activity over the homogeneous control. **MOZ-7** with pendant (*p*-chloro-phenyl)amide groups was similarly designed and optimized for the photocatalytic water oxidation reaction (WOR) with a TON of 10,213. Importantly, a combination of **MOZ-4** and **MOZ-7** with $Co(bpy)_3^{2+}$ (bpy, 2,2′-bipyridine) as a redox mediator achieved total artificial photosynthesis of $(1+n)CO_2 + 2H_2O \rightarrow CH_4 + nCO + (2+n/2)O_2$ through a Z-scheme to afford a turnover frequency (TOF) of 98.7 h^{-1}, outperforming previously reported photocatalysts by over an order of magnitude.

Results

MOZs for photocatalytic carbon dioxide reduction

We first designed a MOZ library for photocatalytic CO_2RR (Fig. 2). An underlying monolayer MOF (Hf-Ir) incorporating an Ir-based photosensitizer was first synthesized through a solvothermal reaction, which afforded the previously reported Hf_{12} clusters[16] $[Hf_{12}(\mu_3\text{-}O)_8(\mu_3\text{-}OH)_8(\mu_2\text{-}OH)_6]$ vertically capped by trifluoroacetate (TFA) and laterally connected by photosensitizing Ir(4,4′-di(4-benzoato)-2,2′-bipyridine)[2-(2,4-difluorophenyl)-5-(trifluoromethyl)pyridine]$_2^+$ (Ir-PS) ligands (Supplementary Note 1). The crystalline two-dimensional network of the formula $Hf_{12}(\mu_3\text{-}O)_8(\mu_3\text{-}OH)_8(\mu_2\text{-}OH)_6$(Ir-PS)$_6(TFA)_6$ (Supplementary Fig. 1) consists of Hf_{12} clusters capped with six labile TFA groups, which can be exchanged for more strongly coordinating carboxylate groups to incorporate various functional groups onto these MOZs (Supplementary Note 2). Through carboxylate exchange, the ferric protoporphyrin haemin was installed onto Hf-Ir to afford a primary MOZ (**MOZ-1**), including an active Fe-based metal centre.

MOZ-1 retained the monolayer morphology of Hf-Ir with a diameter of ~150 nm and a thickness of ~2.1 nm, as determined by transmission electron microscopy (TEM; Fig. 3a) and atomic force microscopy (AFM; Fig. 3d), respectively. The ~0.5 nm increase in thickness of **MOZ-1** over Hf-Ir corroborated the expected increase in the height for Hf_{12} clusters modified with flexible haemin groups. High-resolution TEM (HRTEM; Fig. 3a, inset) and high-angle annular dark-field (HAADF; Fig. 3b) imaging of **MOZ-1** revealed a preserved sixfold **kgd** topological structure and the expected Hf_{12}–Hf_{12} distance of ~2.8 nm. This topological structure of **MOZ-1** was further supported by comparing its powder X-ray diffraction pattern to that simulated from its model structure (Fig. 3f). Energy-dispersive X-ray spectroscopy (EDS) mapping showed homogeneous distribution of haemin groups over the Hf- and Ir-based monolayer (Fig. 3c and Supplementary Fig. 2). The loading of haemin was found to be ~8.0% per Ir-PS based on ultraviolet–visible (UV–vis) absorptions (Fig. 3e and Supplementary Fig. 3) by deconvoluting the spectrum of digested **MOZ-1** into absorptions from haemin and from Ir-PS, affording an empirical formula of $Hf_{12}(\mu_3\text{-}O)_8(\mu_3\text{-}OH)_8(\mu_2\text{-}OH)_6$(Ir-PS)$_6$(haemin)$_{0.48}(TFA)_{5.52}$ for **MOZ-1** (Supplementary Note 3). The ratio of haemin to Ir-PS was designed to be <10% so multiple electrons could be injected from Ir-PSs into haemin during a CO_2RR catalytic cycle. Moreover, the remaining TFA (~90%) accommodated further modification of **MOZ-1** with AAs.

MOZ-1 was subsequently diversified by replacing the remaining TFA groups with proteinogenic AAs to generate a library of MOZs (Fig. 2). Prototypical Glu- and Asn-modified MOZs (denoted **MOZ-2** and **MOZ-3**, respectively) were specifically selected for comprehensive characterization. These MOZs again maintained the topological structure of **MOZ-1**, as revealed by powder X-ray diffraction (Fig. 3f) and HRTEM imaging (Supplementary Fig. 4). Moreover, TEM, AFM and dynamic light scattering (DLS) revealed a preserved monolayer morphology, with diameters of ~150 nm, thicknesses of 2.0–2.2 nm and number-averaged sizes of 112–125 nm (Supplementary Fig. 4). The incorporation of Glu and Asn was confirmed by infrared (IR) spectroscopy in which the absorption peaks of **MOZ-1** were consistently observed and the unique spectroscopic features of Glu and Asn were only observed in **MOZ-2** and **MOZ-3**, respectively (Fig. 3g). The exchange of TFA by Glu and Asn was confirmed by NMR analysis of digested haemin-free MOZ analogues, where no TFA signal was observed by ^{19}F NMR and a near 1:1 ratio of AA to Ir-PS signal by ^{1}H NMR. (Note: haemin-free analogues were used to avoid the influence of paramagnetic haemin; Supplementary Fig. 5.) Thus, the weakly coordinating TFA groups were completely replaced by AAs while the strongly coordinating haemin groups remained unchanged, as evidenced by preserved haemin to Ir-PS ratios of 7.8% and 8.0% in Glu- and Asn-modified MOZs, respectively, as quantified through UV–vis analysis (Supplementary Fig. 3). The empirical formulae of **MOZ-2** and **MOZ-3** were therefore determined to be $Hf_{12}(\mu_3\text{-}O)_8(\mu_3\text{-}OH)_8(\mu_2\text{-}OH)_6$(Ir-PS)$_6$(haemin)$_{0.47}(Glu)_{5.53}$ and $Hf_{12}(\mu_3\text{-}O)_8(\mu_3\text{-}OH)_8(\mu_2\text{-}OH)_6$(Ir-PS)$_6$(haemin)$_{0.48}(Asn)_{5.52}$, respectively (Supplementary Note 3). The remaining proteinogenic amino acids are presumed to display similar compositions in their corresponding MOZs.

The MOZs in this library were next selected for photocatalytic CO_2RR activity[17–22]. The proximal arrangements of AAs and Fe–porphyrin centres (that is, haemin) in each MOZ provided unique active sites on each Hf_{12} cluster, with approximately two AAs (and their R groups) within several ångstroms of the Fe centres. The active sites of these MOZs have smaller footprints (sizes) than most natural enzymes (~35 versus ~60 nm^3 per active site; Supplementary Fig. 6 and Supplementary Note 4). MOZs (0.1 μM based on haemin and 1.25 μM based on Ir-PS) were individually added to 1 ml dimethylacetamide (DMA, providing good dispersity of MOZs) solutions of trifluoroethanol (TFE, 100 mM, as proton resource with a proper pK_a of 12.5) and 1,3-dimethyl-2-phenyl-2,3-dihydro-1*H*-benzo[d]-imidazole (BIH, 50 mM, as sacrificial reductant) under 1 atm CO_2 and at room temperature, with visible-light irradiation for 6 h (Xenon lamp, $\lambda > 300$ nm). On irradiation, photoexcited Ir-PS ligands can inject electrons into the active sites of each MOZ to drive CO_2RR. MOZ-catalysed CO_2RR produces CO and CH_4 through two distinct steps: first, reduction of CO_2 to CO through a two-electron and two-proton process; second, reduction of CO to CH_4 through a six-electron and six-proton process (Supplementary Fig. 8). The production of CO and CH_4 was detected by both gas chromatography (GC; Supplementary Fig. 9) and gas chromatography–mass spectrometry (GC–MS; Supplementary Fig. 10)

Fig. 1 | Design of MOZs. a, Schematic of the natural enzyme cytochrome P450 74A (PDB 3DSI) and its active site[1] where substrate is bound to the haem and stabilized in the secondary coordination sphere by an adjacent Asn residue. The overall reaction is promoted by the NAD(P)H cofactor. **b**, Schematic of representative MOZs reported in this work for CO_2RR and WOR with their active sites. The overall reaction is promoted by photoexcited Ir-PS cofactors. By combining these MOZs in a single photocatalytic system, total artificial photosynthesis is realized by converting CO_2 and H_2O into CH_4/CO and O_2. Hydrogen atoms bound to carbon are omitted for clarity. C atoms in haem are highlighted in green with all other atoms labelled as follows: H, white; C, grey; O, red; N, blue; Fe, orange in haemin; Hf, light blue; Ir, yellow in Ir-PS, orange in MBA-Ir*. **c**, Schematic showing diversification, selection and optimization of MOZs. These three steps correspond, in order, to diversification and designing MOZ templates inspired by biocatalysts to create a library of MOZs through the incorporation of amino acids, followed by selection and screening of these MOZs for specific and enhanced activity and then optimization and elucidating how this activity is enhanced allowing for the design of artificial ligands with increased functionality.

https://doi.org/10.1038/s41929-022-00865-5

and the corresponding mechanism was determined by a combination of isotope labelling (Supplementary Fig. 11), kinetic study (Supplementary Fig. 12), luminescence quenching (Supplementary Fig. 13), time-resolved luminescence spectroscopy (Supplementary Fig. 14), cyclic voltammetry (Supplementary Fig. 15), electron paramagnetic resonance spectroscopy (Supplementary Fig. 16) and IR spectroscopy (Supplementary Fig. 17)[17,23,24]. The detailed discussions are provided in Supplementary Notes 5–8. The only observed by-product of this

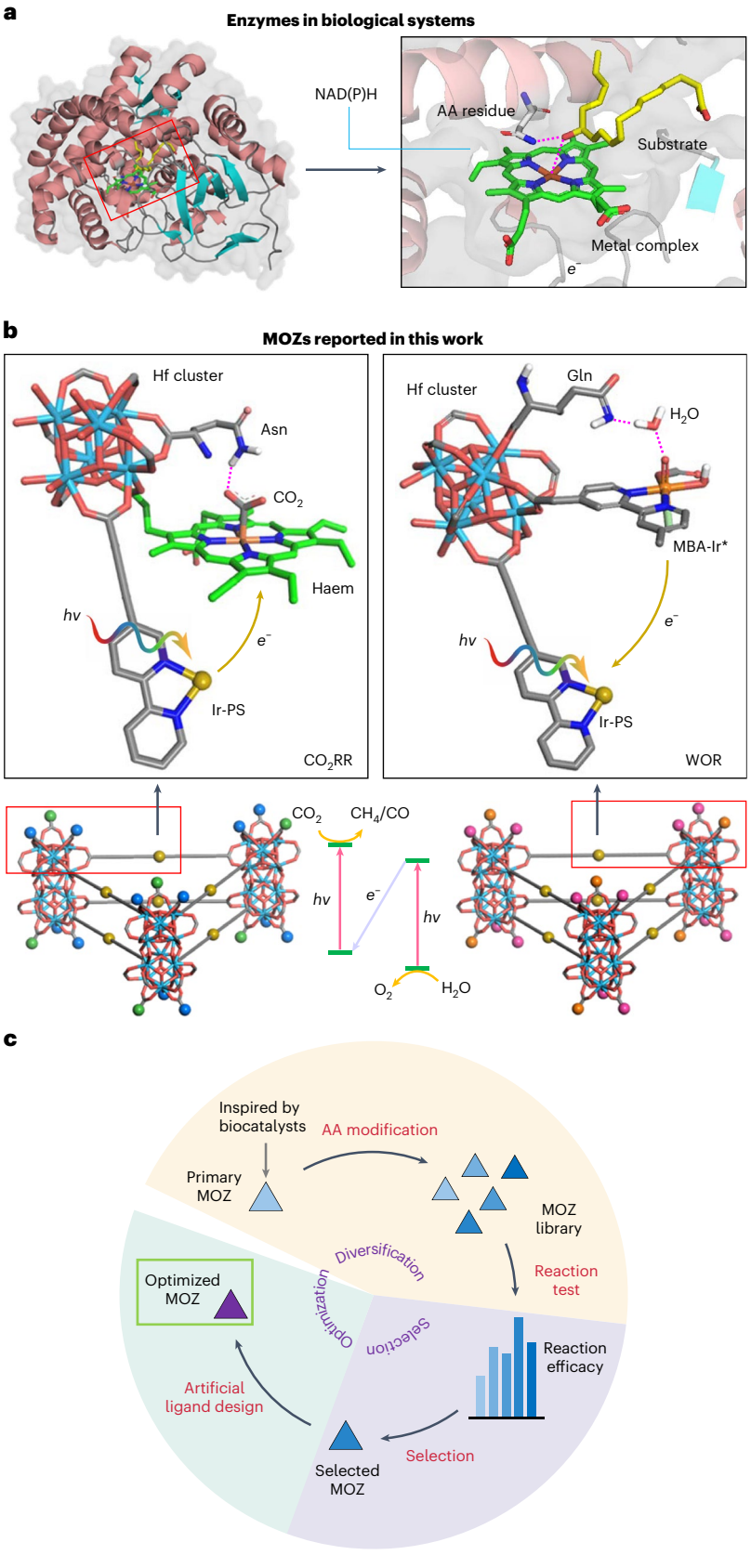

https://doi.org/10.1038/s41929-022-00865-5

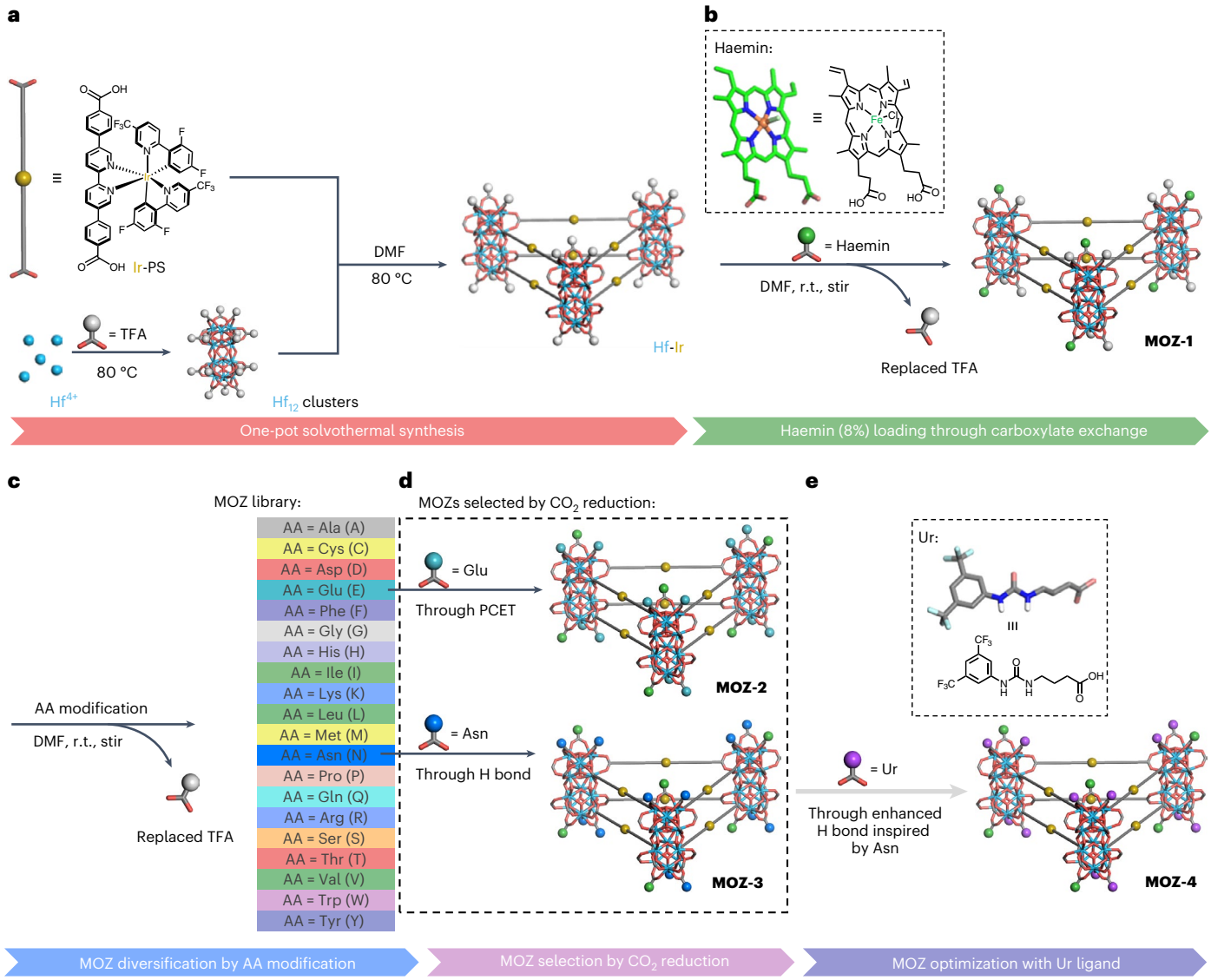

Fig. 2 | MOZ construction and optimization for CO_2RR. a, Hf-Ir monolayer was synthesized through a one-pot solvothermal synthesis to interlink Hf_{12} secondary building units with Ir-PS. **b**, **MOZ-1** was synthesized through post-synthetic modification of Hf-Ir monolayer with haemin, wherein weakly coordinated TFA is replaced through carboxylate exchange. r.t., room temperature. **c**, The library of MOZs was generated by separately appending 20 AAs on **MOZ-1**, whereby all remaining TFA was exchanged to generate 20 MOZ candidates with unique active sites. **d**, **MOZ-2** (with Glu modification) and **MOZ-3** (with Asn modification) showed enhanced activity for photocatalytic CO_2 reduction by promoting PCET and stabilization of reactive intermediates through hydrogen bonding, respectively. **e**, Inspired by hydrogen-bonding interactions in **MOZ-3**, the Ur ligand (capable of stronger bonding) was designed and synthesized. The optimized **MOZ-4** was generated by appending this Ur ligand onto **MOZ-1** and showed the highest activity for photocatalytic CO_2RR.

reaction is H_2, which is proposed to proceed through a competing reaction pathway[17,24]. The activity of each MOZ for CO_2RR was evaluated by quantifying the generation of CO and CH_4. **MOZ-1** showed a sevenfold increase in TON compared to the homogeneous control (a molar-equivalent mixture of haemin and Ir-PS) owing to accelerated electron transfer from excited Ir-PSs to the adjacent haemin (<2 nm distance) (Fig. 4b, Supplementary Fig. 12f and Supplementary Note 9). AA-modified MOZs, particularly **MOZ-2** and **MOZ-3**, can further enhance these CO_2RR activities. This enhancement is proposed to proceed through two distinct pathways: proton-coupled electron transfer (PCET) and hydrogen-bond (H-bond) stabilization (Fig. 4a).

First, as the generation of both CO and CH_4 requires protons and electrons, MOZs with R groups more acidic (that is, lower pK_a) than the provided proton source (TFE, pK_a = 12.5) may enhance activity through a PCET pathway[25]. This is quantified by plotting the TONs for both CH_4 and CO generation against the pK_a values of R groups on individual MOZs, with Pearson correlation coefficients of −0.97 and −0.99, respectively (Supplementary Fig. 18). The enhancement of CO_2RR via this PCET pathway is maximized in Glu-modified **MOZ-2**, as Glu displays the lowest pK_a value among proteinogenic AAs. MOZs modified with AAs whose R groups were 'less' acidic than TFE were not expected to exhibit higher activity than **MOZ-1**, and so we were surprised to discover that Asn- and Gln-modified MOZs afforded much higher CO_2RR activity over even **MOZ-2** (Fig. 4a). We propose that this enhancement by Asn and Gln arises through H-bond stabilization, specifically through secondary coordination sphere interactions between electron-deficient amide –NH fragments and Fe-bound reactive intermediates (Fig. 1b)[26]. This enhancement in CO_2RR activity via H-bond stabilization is maximized in Asn-modified **MOZ-3**.

The H-bond stabilization by **MOZ-3** was elucidated by density functional theory (DFT) calculations. In the proposed two-step reduction of CO_2 and CO, $Fe^{II}CO_2^{2-}$ and $Fe^{I}CHO$ are proposed as crucial reactive

https://doi.org/10.1038/s41929-022-00865-5

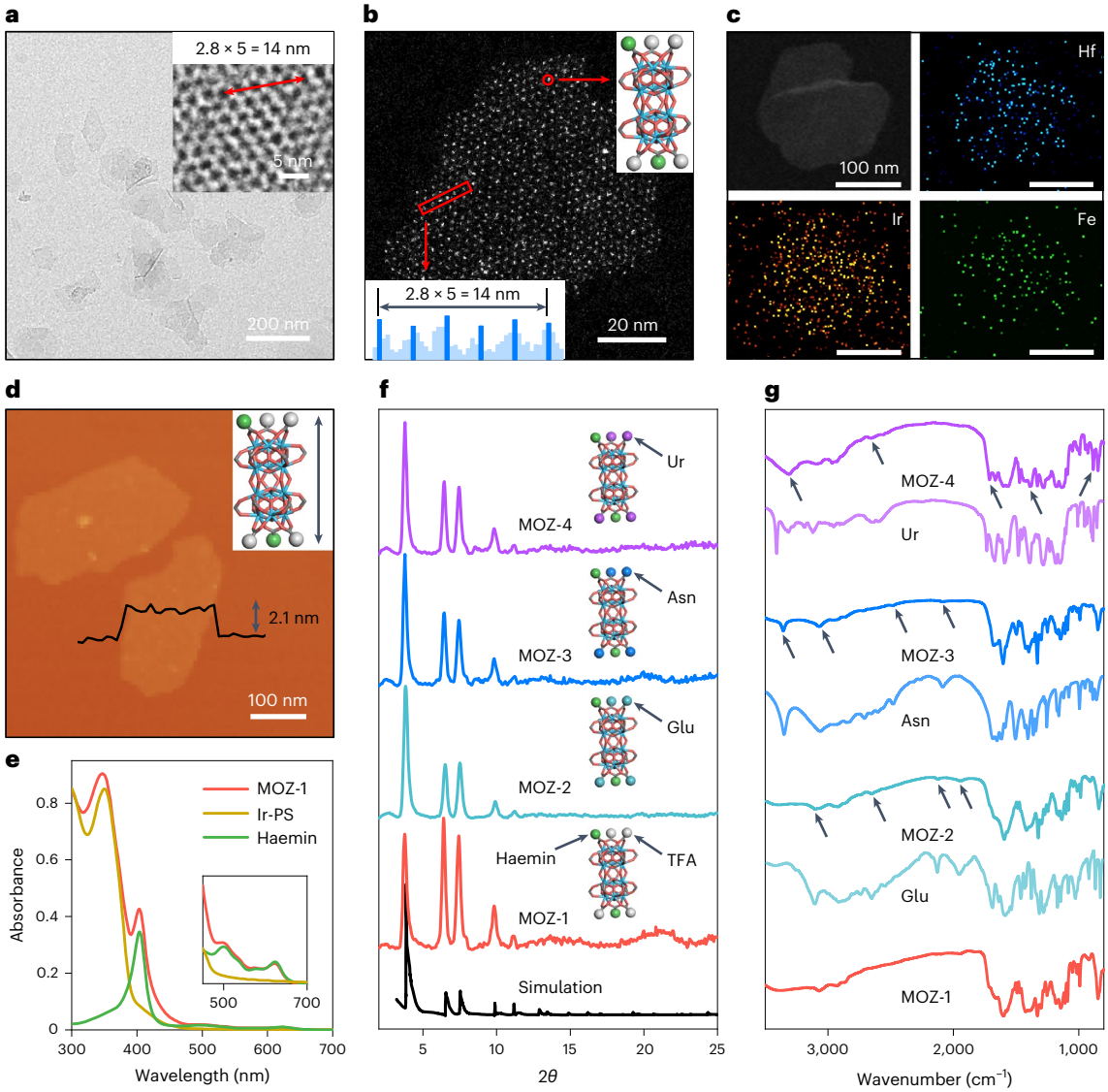

Fig. 3 | Characterization of MOZs. a–d, TEM and HRTEM (inset) images (**a**), HAADF image (**b**), EDS maps (**c**) and AFM topography (**d**) with height profile of **MOZ-1**. Haemin-capped Hf_{12} clusters appear as black and white regions in **a** and **b**, respectively. **e**, UV–vis spectrum of digested **MOZ-1** and its deconvolution into haemin and Ir-PS absorptions. **f**, Powder X-ray diffraction patterns of MOZs compared to the simulated pattern based on the underlying monolayered MOF structure. Haemin-capped Hf_{12} clusters with various capping groups (that is, TFA, Glu, Asn and Ur) are also shown to illustrate different MOZs. **g**, IR spectra of MOZs compared to corresponding Glu, Asn and Ur absorptions. Black arrows in **MOZ-2**, **MOZ-3** and **MOZ-4** spectra correspond to Glu, Asn and Ur, respectively.

intermediates (Fig. 4c). DFT calculations were thus performed on model compounds to investigate the possible geometries of $Fe^{II}CO_2^{2-}$ and $Fe^{I}CHO$ (Supplementary Fig. 19 and Supplementary Note 10)[27]. **MOZ-3** showed a moderate H-bond interaction between amide groups and Fe-bound CO_2 in $Fe^{II}CO_2^{2-}$, with an (N)H···O donor–acceptor distance of 1.96 Å and corresponding free enthalpy of stabilization (ΔH_{Stb}) of −14.1 kcal mol^{-1} (Fig. 4c). **MOZ-3** showed an additional moderate H-bond interaction between amide groups and the Fe-bound CHO in $Fe^{I}CHO$, with an (N)H···O donor–acceptor distance of 2.02 Å and a corresponding ΔH_{Stb} of −9.1 kcal mol^{-1} (Fig. 4c).

The activities of these MOZs were further evaluated in time-dependent reactions. On 72 h of visible-light irradiation, **MOZ-2** and **MOZ-3** significantly enhanced CO_2RR, with the TONs for CO/CH_4 reaching 9,530 ± 753/4,248 ± 232 and 14,620 ± 995/5,740 ± 414, respectively, compared to 3,849 ± 137/2,213 ± 26 for **MOZ-1** and only 955 ± 262/373 ± 47 for the homogeneous control (Fig. 4b and Supplementary Fig. 20a). **MOZ-2**, however, was only moderately selective for CO_2RR (80.9%), as the PCET pathway enabled by Glu also accelerated the generation of H_2 (Fig. 4d and Supplementary Fig. 20a,b). In contrast, **MOZ-3** accelerated the sequential generation of CO and CH_4 by stabilizing their reactive intermediates, leaving the H_2 generation pathway unaffected, thus leading to an enhanced selectivity of 97.4% (Fig. 4d and Supplementary Fig. 20a,b).

The activity of this library in CO_2RR was optimized by designing a urea-based ligand (Ur) to provide even stronger H-bond stabilization. This Ur ligand includes a phenyl ring bearing two electron-withdrawing $-CF_3$ groups to enhance the H-bond donor strength of the urea –NH fragment (Supplementary Fig. 21 and Supplementary Data 2). Ur was modified onto **MOZ-1** in the same manner as above to afford **MOZ-4** and was similarly characterized to reveal a conserved morphology, topography and structure, with the empirical formula $Hf_{12}(\mu_3\text{-}O)_8(\mu_3\text{-}OH)_8(\mu_2\text{-}OH)_6$(Ir-PS)$_6$(haemin)$_{0.46}(Ur)_{5.54}$ (Supplementary Figs. 3–5). As desired, **MOZ-4** further enhanced CO_2 reduction with TONs for CO/H_4 of 24,740 ± 649/10,352 ± 592 and a selectivity for CO_2RR of 98.0% over 72 h of visible-light irradiation, a fivefold increase in activity over **MOZ-1** and 27-fold increase in activity over the homogeneous control

https://doi.org/10.1038/s41929-022-00865-5

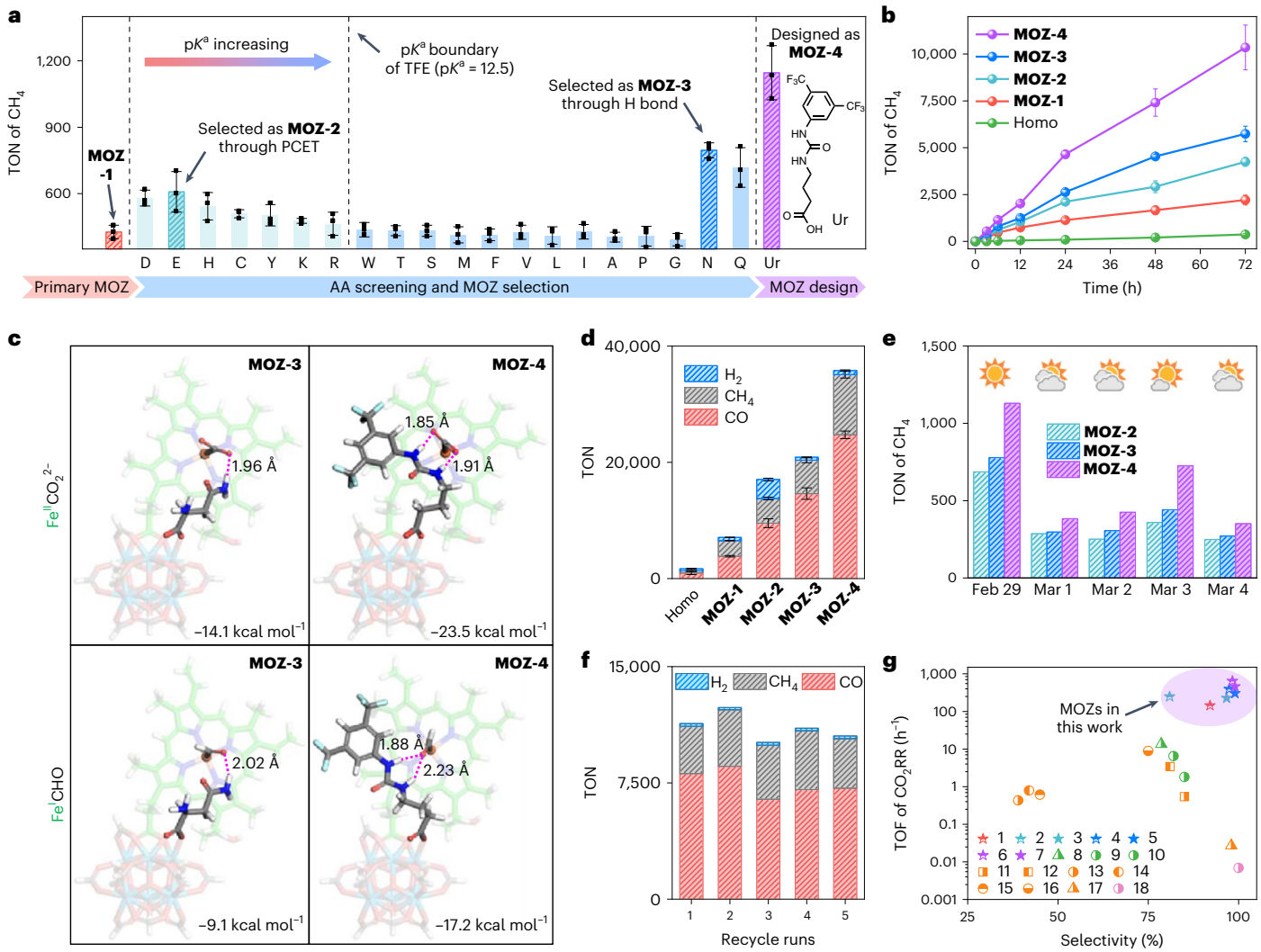

Fig. 4 | Photocatalytic CO_2RR by MOZs. a, TONs for CH_4 of **MOZ-1**, AA-modified MOZs and Ur-modified MOZ. AAs are represented with one-letter codes and inset shows the structure of Ur. Data are presented as mean ± s.d. ($n = 3$) with the error bars representing the s.d.; individual data points are shown as black dots. **b**, Time-dependent TONs of CH_4 for MOZs and homogeneous control (Homo) under visible-light irradiation. Data are presented as mean ± s.d. ($n = 3$) with the error bars representing the s.d.; individual data points are shown as black dots. **c**, Representative model structures of $Fe^{II}CO_2^{2-}$ and $Fe^{I}CHO$ in **MOZ-3** and $Fe^{II}CO_2^{2-}$ and $Fe^{I}CHO$ in **MOZ-4**, optimized by DFT calculation at (U)B3LYP-D3 level of theory with a simplified Zr_6 cluster (Supplementary Fig. 19, Supplementary Note 11 and Supplementary Data 1). C atoms in haem are labelled in green, with all other atoms labelled as follows: H, white; C, grey; O, red; N, blue; F, cyan; Fe, orange; Zr, light blue. Fe-bound CO_2, Fe-bound CHO, Asn and Ur are highlighted. Hydrogen bonds are presented as magenta dotted line with their bond distances labelled alongside and corresponding stabilized enthalpy (ΔH_{Stb}) detailed in the bottom right corners. **d**, TON summary of CO, CH_4 and H_2 for MOZs and homogeneous control under 72 h visible-light irradiation. Data are presented as mean ± s.d. ($n = 3$) with the error bars representing the s.d. **e**, TONs of CH_4 for **MOZ-2**, **MOZ-3** and **MOZ-4** over five consecutive days under direct sunlight. **f**, Summary of TONs of CO, CH_4 and H_2 for recycled **MOZ-4** over five consecutive trials. **g**, Summary of activities for photocatalytic conversion of CO_2 to CH_4 by MOZs in this work compared to previously reported catalysts. Data points 1–7 refer to this work: 1, **MOZ-1**; 2, **MOZ-2**; 3, **MOZ-2** under direct sunlight; 4, **MOZ-3**; 5, **MOZ-3** under direct sunlight; 6, **MOZ-4**; and 7, **MOZ-4** under direct sunlight. Data points 8–10 refer to molecular catalysts: 8, homogeneous control in this work; 9, Fe-*p*-TMA with $Ir(ppy)_3$ (ref. [17]); 10, Fe-*p*-TMA with organic photosensitizer[24]. Data points 11–17 refer to metal and metal oxide nanoparticle-based catalysts: 11, $Pt@Cu_2O/TiO_2$ (ref. [28]); 12, $(MgO,Pt)/TiO_2$ (ref. [29]); 13, Ag/TiO_2 (ref. [29]); 14, Pd/TiO_2 (ref. [29]); 15, Rh/TiO_2 (ref. [29]); 16, Pt/TiO_2 (ref. [30]); 17, Pd_7Cu_1/TiO_2 (ref. [31]). Data point 18 refers to MOF-based catalyst $Cu_3(BTC)_2@TiO_2$ (ref. [32]). All reactions were performed under visible light, except where specifically noted. Detailed reaction conditions and additional catalysts are provided in Supplementary Table 1.

(Fig. 4b,d). This stable, heterogeneous **MOZ-4** was recycled at least five times without apparent loss of activity (Fig. 4f).

The enhancement in activity of **MOZ-4** over **MOZ-3** is attributed to the designed stronger H-bond stabilization, as elucidated by DFT calculations (Supplementary Fig. 19 and Supplementary Note 10). Two strong H bonds to the $Fe^{II}CO_2^{2-}$ intermediate were modelled, with (N)H···O donor–acceptor distances of 1.85 Å and 1.91 Å, and a corresponding ΔH_{Stb} of −23.5 kcal mol^{-1} (Fig. 4c), whereas two strong/moderate H bonds to $Fe^{I}CHO$ intermediates were modelled, with (N)H···O donor–acceptor distances of 1.88 Å and 2.23 Å, and a corresponding ΔH_{Stb} of −17.2 kcal mol^{-1} (Fig. 4c). To confirm H-bond interaction from Ur in **MOZ-4**, we designed analogous ligands with either a single –NH fragment (Am-1) or no –NH fragment (Am-2). As expected, a MOZ modified with the Am-1 ligand showed comparable CO_2RR reactivity to **MOZ-3**, which also contained a single –NH fragment. Moreover, a MOZ modified with the Am-2 ligand showed comparable CO_2RR reactivity to **MOZ-1**, which also was devoid of –NH fragments (Supplementary Fig. 23 and Supplementary Note 11).

MOZ-4 was examined for CO_2RR with energy input from natural sunlight. These photocatalytic CO_2RR studies were carried out

https://doi.org/10.1038/s41929-022-00865-5

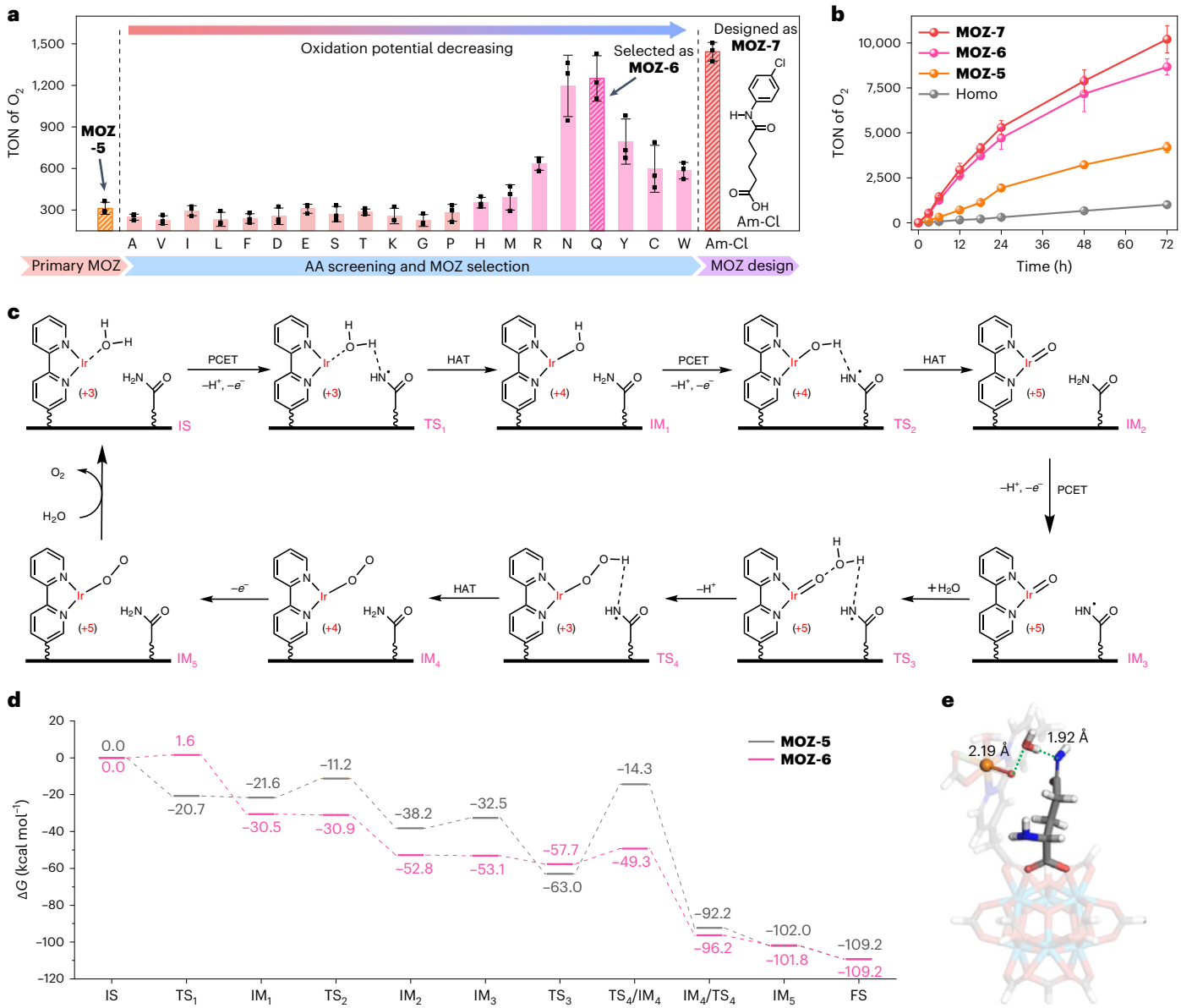

Fig. 5 | Photocatalytic WOR by MOZs. a, TONs for O_2 of **MOZ-5**, AA-modified MOZs and Am-Cl-modified MOZ. Data are presented as mean ± s.d. ($n = 3$) with the error bars representing the s.d.; individual data points are shown as black dots. **b**, Time-dependent TONs of O_2 for MOZs and homogeneous control (Homo) under visible-light irradiation. Data are presented as mean ± s.d. ($n = 3$) with the error bars representing the s.d.; individual data points are shown as black dots. **c**, Proposed mechanism for **MOZ-6**-catalysed WOR. IS, initial state; TS, transitional state; IM, intermediate; FS, final state. **d**, Energy diagram of MOZ-catalysed WOR. **e**, Representative model structure of TS_3 of **MOZ-6**-catalysed WOR. All atoms are labelled as follows: H, white; C, grey; O, red; N, blue; Ir, orange; Zr, light blue; Cl, light green. Ir-bound oxo, H_2O and Gln are highlighted.

under the same conditions as described above under natural sunlight for five consecutive days (Fig. 4e and Supplementary Fig. 20c,d). Reactivity was weather dependent, but on a sunny day, **MOZ-4** catalysed CH_4 generation with a TON of 904, a TOF of 150.7 h^{-1}, a quantum yield of 1.8% at 350 nm and a selectivity of over 99%. **MOZ-4** thus directly converted CO_2 to CH_4 with energy input from sunlight. The MOZs reported in this work showed orders-of-magnitude higher activity and selectivity than recently reported state-of-the-art photocatalysts, including small molecules[17,24], metal and metal oxide nanoparticles[28–31] and MOFs[32], among others (Fig. 4g and Supplementary Table 1).

MOZs for photocatalytic water oxidation

A separate photocatalytic MOZ library for the WOR was constructed and optimized through the same strategy (Supplementary Fig. 24)[33]. A new primary MOZ was constructed from an identical Hf-Ir monolayer with the incorporation of an Ir-based active metal centre (**MOZ-5**). This active catalyst, [Ir(H-MBA)Cp*Cl]$^+$ (MBA-Ir, H-MBA, 2-(4′-methyl-[2,2′-bipyridin]-4-yl)acetic acid; Cp*, pentamethylcyclopentadienyl), was loaded onto the surface of the underlying monolayer at an 8% ratio per Ir-PS (Supplementary Figs. 25 and 26). **MOZ-5** retained the monolayer morphology of Hf-Ir with a diameter of ~150 nm, a thickness of ~2.1 nm and a number-averaged size of 117.4 ± 8.1 nm, as determined by TEM, AFM and DLS, respectively (Supplementary Fig. 25a). HRTEM imaging of **MOZ-5** revealed the six-fold **kgd** topological structure and an expected Hf_{12}–Hf_{12} distance of ~2.8 nm. The topological structure of **MOZ-5** was further supported by the similarity of its powder X-ray diffraction pattern to that simulated from its model structure (Supplementary

https://doi.org/10.1038/s41929-022-00865-5

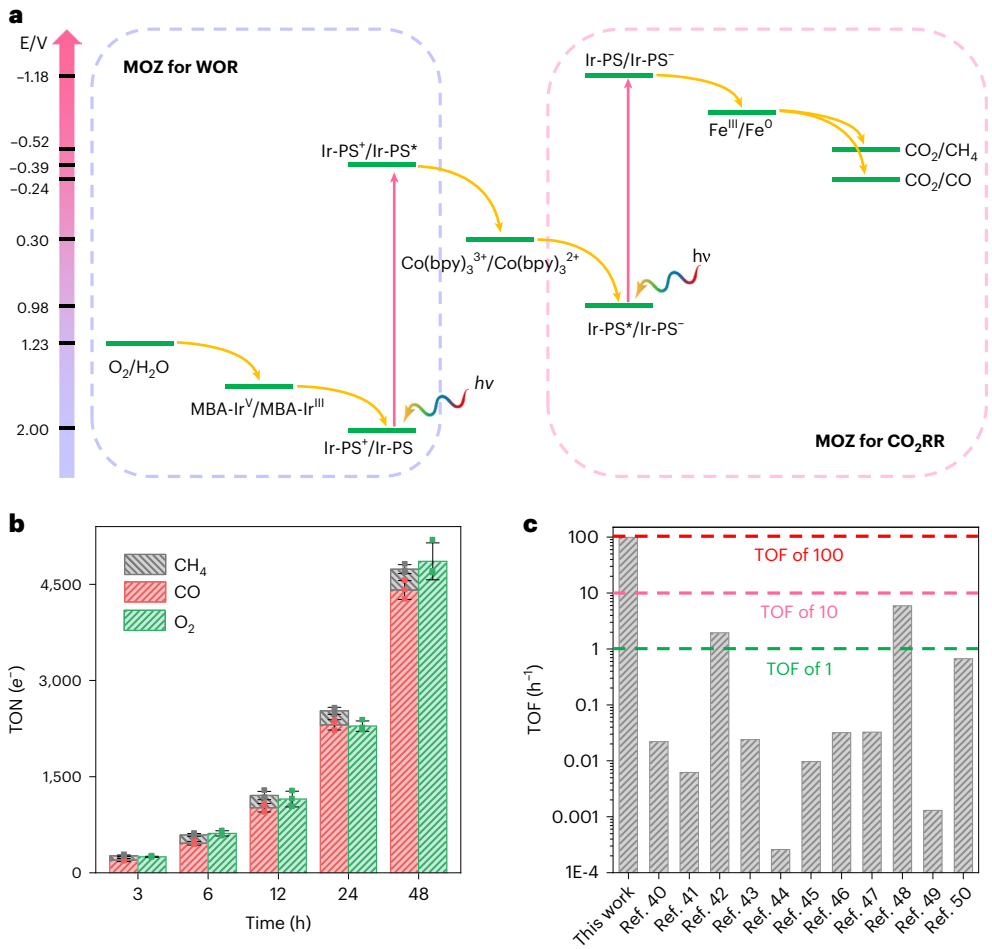

Fig. 6 | Artificial photosynthesis by MOZs. a, Energy-level diagram of a Z-scheme system for photocatalytic total CO_2RR by MOZs. **b**, Time-dependent TONs of CO, CH_4 and O_2 for photocatalytic total CO_2RR by a combination of **MOZ-4** and **MOZ-7**. Data are presented as mean ± s.d. ($n = 3$) with the error bars representing the s.d.; individual data points are shown as dots. **c**, Comparison of photocatalytic total CO_2RR activity in this work with that of previously reported catalysts.

Fig. 25c). **MOZ-5** had an empirical formula of $Hf_{12}(\mu_3\text{-}O)_8(\mu_3\text{-}OH)_8(\mu_2\text{-}OH)_6(Ir\text{-}PS)_6(MBA\text{-}Ir)_{0.48}(TFA)_{5.52}$.

As previously reported[34], MBA-Ir catalyses WOR through two distinct steps: first, the generation of active WOR catalyst $[Ir(MBA)(H_2O)_2(CH_3COO)Cl]^+$ (MBA-Ir*; Supplementary Fig. 28c) via oxidation of the Cp* group; second, the WOR catalysed by MBA-Ir* through an Ir^{III}/Ir^{V} cycle (Supplementary Fig. 28f and Supplementary Note 13). On irradiation, photoexcited Ir-PS oxidizes MBA-Ir to oxidize H_2O to O_2 through a four-electron and four-proton process.

A library of MOZs was subsequently diversified by appending various proteinogenic AAs on **MOZ-5** and selected for photocatalytic WOR activity (Fig. 5a, Supplementary Fig. 27 and Supplementary Notes 12 and 13). The new MOZs were constructed by replacing the remaining TFA on **MOZ-5** with proteinogenic AAs through carboxylate exchange reactions. The resultant MOZ with Gln modification, denoted **MOZ-6**, was characterized by TEM, AFM and DLS, revealing a preserved monolayer morphology, with diameters of ~150 nm, thicknesses of 2.1 nm and number-averaged sizes of 120.6 ± 4.1 nm (Supplementary Fig. 25b). **MOZ-6** also maintained the topological structure of **MOZ-5**, as revealed by powder X-ray diffraction (Supplementary Fig. 25c) and HRTEM imaging. The incorporation of Gln in **MOZ-6** was confirmed by NMR analysis of digested **MOZ-6** with a near 1:1 ratio of Gln to Ir-PS signal. While weakly coordinating TFA groups could be completely replaced by AAs, strongly coordinating MBA-Ir groups remained unchanged, affording a formulation of $Hf_{12}(\mu_3\text{-}O)_8(\mu_3\text{-}OH)_8(\mu_2\text{-}OH)_6(Ir\text{-}PS)_6(MBA\text{-}Ir)_{0.48}(Gln)_{5.52}$ for **MOZ-6** (Supplementary Fig. 25e).

Enhanced activities for WOR were achieved with AA-modified MOZs with cationic AA radicals ($AA^{\bullet+}$) that exhibit oxidation potentials between 1.24 and 1.77 V. This WOR activity enhancement was maximized in Gln-modified **MOZ-6** (Supplementary Fig. 28e) and a volcano plot was obtained by plotting the WOR activity against the oxidation potential of $AA^{\bullet+}/AA$. These results suggest that here AAs may function as electron mediators for WOR via photo-oxidation of the proximal AA by Ir-PS to form $AA^{\bullet+}$ through a PCET pathway, followed by the oxidation of H_2O-bound MBA-Ir* by $AA^{\bullet+}$ through hydrogen atom transfer (HAT) (Supplementary Fig. 28d). The proposed WOR mechanism of **MOZ-6** is shown in Fig. 5c with its energy diagram calculated by DFT (Fig. 5d and Supplementary Note 14). In this proposed mechanism, the rate-determining step of MBA-Ir* catalysed WOR is the formation of the oxygen–oxygen bond (corresponding to IM_2 to IM_4 in Fig. 5c), in which the activation energy drops from 48.7 kcal mol^{-1} in **MOZ-5** to 8.4 kcal mol^{-1} in **MOZ-6**. To further clarify the formation of the oxygen–oxygen bond, the geometry of TS_3 in **MOZ-6** was optimized by DFT calculations (Fig. 5e). These calculations revealed bound H_2O molecules could be stabilized by $Gln^{\bullet+}$ through a H-bond interaction (1.92 Å) placing the oxygen atom within range (2.19 Å) for attack of proximal Ir^{V}=O moieties to form the oxygen–oxygen bond along with HAT from H_2O to $Gln^{\bullet+}$. As a result, **MOZ-6** significantly enhances WOR with a 72 h TON for O_2 generation reaching 8,679 ± 446, compared to 4,196 ± 289 for **MOZ-5** and only 1,006 ± 171 for the homogeneous control (Fig. 5b).

To further validate the proposed function of AAs as electron mediators in WOR, we designed a series of artificial ligands (Am-R) derived from 6-oxo-6-(phenylamino)hexanoic acid to optimize MOZ reactivity (Supplementary Fig. 29). The Am-R ligands (R = OCH_3, CH_3, F, H, Cl, Br or NO_2) were composed of the same amide group but with oxidization potentials that could be tuned with the functional groups attached to the phenyl ring. By modifying **MOZ-5** with these artificial ligands, a similar volcano plot to that above was constructed by plotting the WOR activity against the oxidation potential. The WOR activity was optimized with Am-Cl (R = Cl) in **MOZ-7** (Fig. 5a, Supplementary Fig. 29 and Supplementary Notes 15 and 16) with a 72 h TON of 10,213 ± 758 (Fig. 5b). **MOZ-7** showed higher photocatalytic WOR activity than many previously reported catalysts (Supplementary Table 2)[35–38].

MOZs for photocatalytic total carbon dioxide reduction

Combining these two libraries, photocatalytic total CO_2RR was realized through a Z-scheme system relying on **MOZ-4** and **MOZ-7** for CO_2RR and WOR, respectively, with $Co(bpy)_3^{2+}$ as a redox mediator (Fig. 6a). To improve reactivity, we first optimized the concentration of $Co(bpy)_3^{2+}$ as a redox mediator. Reactions were performed for 6 hours and the calculated TOF of CO_2RR (CO + CH_4) achieved a maximum of 18.4 h^{-1} with 30 μM $Co(bpy)_3^{2+}$ (Supplementary Fig. 30a). We next optimized the ratio of **MOZ-4** and **MOZ-7** to match the reaction rate of both CO_2RR and WOR for higher activity. The highest TOF of total CO_2RR was found with a **MOZ-4** to **MOZ-7** ratio of 1:3 (Supplementary Fig. 30b).

In the absence of any sacrificial reagent, a combination of **MOZ-4** and **MOZ-7** in the optimized 1:3 ratio with 30 μM concentration of $Co(bpy)_3^{2+}$ competently catalysed total photocatalytic CO_2 reduction to afford TONs of 4,412 ± 147, 324 ± 69 and 1,619 ± 96, for CO, CH_4 and O_2, respectively, during 48 hour reactions (Fig. 6b). The quantum yield of MOZ-catalysed photocatalytic total CO_2RR was determined to be 1.1% at 350 nm. As a control, no obvious CO_2RR or WOR products were detected in the homogeneous control (a molar-equivalent mixture of Ir-PS, haemin, Me-MBA-Ir and $Co(bpy)_3Cl_2$) or without $Co(bpy)_3Cl_2$ as mediator. This is probably because MOZs not only integrate CO_2RR or WOR active sites, but also isolate these two active sites into different MOZs to avoid mutual quenching. $Co(bpy)_3Cl_2$ was selected as an electron shuttle between **MOZ-4** ($Ir\text{-}PS^*/Ir\text{-}PS^-$, 0.98 V versus standard hydrogen electrode (SHE)) and **MOZ-7** ($Ir\text{-}PS^+/Ir\text{-}PS^*$, −0.39 V versus SHE) due to its proper redox potential of $[Co(bpy)_3]^{3+}/[Co(bpy)_3]^{2+}$ (0.30 V versus SHE). No obvious CO_2RR or WOR products were detected in a mixture of **MOZ-4** and **MOZ-6** without $Co(bpy)_3Cl_2$. The photocatalytic CO_2RR activity corresponded to a TOF for total artificial photosynthesis of 98.7 ± 3.7 h^{-1}, outperforming previously reported photocatalysts (for example, MOFs and metal oxide nanoparticles) for complete artificial photosynthesis (that is, converting water and CO_2 into O_2 and carbonaceous products using only light) by over an order of magnitude under similar reaction conditions (Fig. 6c and Supplementary Table 3)[39–50].

Conclusions

In this work we reported the rational design of MOF-based artificial enzymes by integrating active metal centres, proximal amino acids and other cofactors into tunable MOF monolayers. Through a diversification–selection–optimization strategy, two libraries of MOZs were developed for photocatalytic CO_2RR and WOR, respectively. When combined into a single system, these MOZs realized efficient artificial photosynthesis in the presence of a catalytic amount of $Co(bpy)_3^{2+}$ redox mediator. We anticipate that the operating principles of our system can be leveraged to develop other MOZs for increasingly challenging reactions (for example, N_2 reduction and complex molecule synthesis) by integrating diverse metal complexes, AAs, peptides, artificial ligands and other cofactors into MOF monolayers.

Methods

Materials

The following solvents and chemicals were used as received: *N*,*N*-dimethylformamide (DMF; 99.9%, Fisher), ethanol (EtOH, 99.5%, Decan), methanol (MeOH, 99.8%, Fisher), chloroform ($CHCl_3$, 99.8%, Fisher), acetonitrile (MeCN, 99.9%, Acros), *N*,*N*-dimethylacetamide (DMA, 99%, Acros), $HfCl_4$ (99%, Acros), (3,5)-bis(trifluoromethyl) phenyl isocyanate (98%, Acros), 4-aminobutyric acid (97%, Alfa Aesar), haemin (Alfa Aesar, 98%), trifluoroethanol (TFE, 99%, Sigma-Aldrich), trifluoroacetic acid (TFA, 99%, Sigma-Aldrich), L-arginine monohydrochloride (98%, Alfa Aesar), L-glutamine (99%, Alfa Aesar), glycine (99%, Thermo Scientific), L-alanine (99%, Alfa Aesar), L-isoleucine (99%, Alfa Aesar), L-methionine (98%, Acros), L-phenylalanine (99%, Alfa Aesar), L-asparagine (98%, Sigma-Aldrich), L-aspartic acid (98%, Sigma-Aldrich), L-cysteine (98%, Sigma-Aldrich), L-glutamic acid (98%, Sigma-Aldrich), L-histidine (98%, Sigma-Aldrich), L-leucine (98%, Sigma-Aldrich), L-lysine (98%, Sigma-Aldrich), L-proline (98%, Sigma-Aldrich), L-serine (98%, Sigma-Aldrich), L-threonine (98%, Sigma-Aldrich), L-tryptophan (98%, Sigma-Aldrich), L-tyrosine (98%, Sigma-Aldrich), L-valine (98%, Sigma-Aldrich), aniline (99%, Fisher Chemical), *p*-bromoaniline (98%, Alfa Aesar), *p*-nitroaniline (98%, Alfa Aesar), *p*-fluoroaniline (99%, Alfa Aesar), *p*-chloroaniline (98%, Alfa Aesar), *p*-toluidine (99%, Alfa Aesar), *p*-anisidine (99%, Alfa Aesar), 1-(3-dimethylaminopropyl)-3-ethylcarbodiimide hydrochloride (98%, Acros Organic), monomethyl adipate (97%, Acros Organic), thionyl chloride (99%, Sigma-Aldrich), lithium hydroxide hydrate (98%, Sigma-Aldrich), d_3-trifluoroethanol (99.5%, Sigma-Aldrich), $H_2{}^{18}O$ (Cortecnet, 99.2%) and $^{13}CO_2$ (Cambridge Isotope Laboratories, 99%).

Ir(4,4′-di(4-benzoato)-2,2′-bipyridine)[2-(2,4-difluorophenyl)-5-(trifluoromethyl) pyridine]$_2^+$ (Ir-PS)[51], 1,3-dimethyl-2-phenyl-2,3-dihydro-1*H*-benzo[d]-imidazole (BIH)[52] and tris(bipyridine)cobalt(II) chloride $[Co(bpy)_3]Cl_2$[53] were synthesized as previously described.

Synthesis of MOZ-1

To a 1 ml DMF suspension of Hf-Ir (4.1 μmol based on Ir) was added 0.267 mg (0.41 μmol) haemin. The reaction mixture was stirred for 3 hours at room temperature. The resultant dark yellow precipitate was collected by centrifugation and washed with DMF three times to quantitatively generate **MOZ-1**.

Amino acid modification and synthesis of MOZ-2, MOZ-3 and MOZ-4

To separate 1 ml DMF suspensions of **MOZ-1** (4.0 μmol based on Ir) 3 equivalents (relative to iridium) of each AA or Ur was added. Each reaction mixture was stirred overnight at room temperature. The resultant dark yellow precipitates were collected by centrifugation and washed with DMF three times to give modified MOZs in quantitative yields. **MOZ-2** and **MOZ-3** were generated from Glu and Asn modification, respectively, and **MOZ-4** was generated from Ur modification.

Synthesis of MOZ-5, MOZ-6 and MOZ-7

To a 1 ml DMF suspension of Hf-Ir (4.1 μmol based on Ir) was added 0.229 mg (0.41 μmol) H-MBA-Ir. The reaction mixture was stirred for 3 hours at room temperature. The yellow precipitate was collected by centrifugation and washed with DMF three times to generate **MOZ-5**. To separate 1 ml DMF suspensions of **MOZ-5** (4.0 μmol based on Ir) were added 3 equivalents relative to iridium of each AA or 6-oxo-6-(phenylamino) hexanoic acid-derived artificial ligand. Each reaction mixture was stirred overnight at room temperature. The yellow precipitates were collected by centrifugation and washed with DMF three times to give modified MOZs. **MOZ-6** was generated from Gln modification, and **MOZ-7** was generated from modification with 6-((4-chlorophenyl)amino)-6-oxohexanoic acid (Am-Cl).

Single-crystal X-ray diffraction

Single-crystal X-ray diffraction was performed with a Bruker APEX II CCD based detector at ChemMatCARS (Sector 15), Advanced Photon Source (APS), Argonne National Laboratory. Data were scaled and corrected for absorption effects using the multiscan procedure as implemented in SADABS (Bruker AXS, v.2014/5, 2015, part of Bruker APEX3 software package). Structures were solved with SHELXT (v.2014/5)[54] and refined by a full-matrix least-squares procedure using OLEX2 (ref. [55]) software packages (XL refinement program v.2014/7)[56].

Transmission electron microscopy

TEM and HRTEM were carried out on a TECNAI Spirit instrument at 120 kV and an F30 instrument at 300 kV, respectively. Samples for TEM were prepared by drop-casting diluted ethanol suspensions of analyte onto carbon-coated copper grids.

Scanning transmission electron microscopy

STEM images were acquired on a JEM-ARM200CF, which is a probe aberration corrected 200 kV STEM/TEM with a cold field emission source and 0.35 eV energy resolution. For HAADF imaging at 200 kV this instrument has a resolution of less than 0.08 nm. Samples for STEM were prepared by drop-casting diluted ethanol suspensions of analytes onto ultrathin carbon-coated copper grids. STEM EDS maps were acquired using an Oxford X-max 100TLE windowless SDD X-ray detector equipped with JEM-ARM200CF. Samples for EDS mapping were also prepared by drop-casting diluted ethanol suspensions of analytes onto carbon-coated nickel grids.

Dynamic light scattering

DLS was carried out on a Malvern Zetasizer Nano ZS instrument. Samples for DLS were prepared from diluted ethanol suspensions of analytes.

Powder X-ray diffraction

Powder X-ray diffraction data were collected on a Bruker D8 Venture diffractometer using a CuKα radiation source (λ = 1.54178 Å). As-synthesized powder metal–organic–zyme (MOZ) samples were used for powder X-ray diffraction analysis after washing with DMF and ethanol and subsequently collecting the analytes via centrifugation.

Atomic force microscopy

AFM images were taken on a Bruker V/Multimode 8 instrument. Samples for AFM were prepared by drop-casting diluted ethanol suspensions of analyte onto freshly peeled mica.

Infrared spectroscopy

IR spectra were recorded in the range of 500–4,000 cm^{-1} on a Thermo NEXUS FT-IR spectrophotometer. Samples for IR were prepared either as pressed KBr pellets or in SL-3 sealed liquid cells equipped with an NaCl window.

Inductively coupled plasma-mass spectrometry

ICP-MS data were obtained with an Agilent 7700x ICP-MS instrument and analysed using ICP-MS Mass Hunter v.B01.03. Digested samples were diluted into a 2% HNO_3 matrix and analysed with a ^{159}Tb internal standard against a 12-point standard curve ranging from 0.1 ppb to 500 ppb. Correlation was >0.9997 for all relevant analyses. Data collection was performed in spectrum mode with five replicates per sample and 100 sweeps per replicate.

Brunauer–Emmett–Teller experiments

Nitrogen sorption studies were performed on a Micromeritics Flex. For each sample 50 mg was activated by a sample preparation system before the N_2 sorption experiments.

Cyclic voltammetry

Cyclic voltammetry spectra were recorded on a CHI420 electrochemistry workstation. Three electrode systems were used. Measurements were recorded using a glassy carbon electrode (S = 0.07 cm^2) and a platinum wire as the counter electrode. An AgCl/Ag electrode in 10 mM $AgNO_3$ 0.1 M electrolyte (NBu_4PF_6) acetonitrile solution was used as the reference electrode, and its potential was calibrated with the Fc^+/Fc couple.

NMR spectroscopy

^1H NMR, ^{13}C NMR and ^{19}F NMR spectra were recorded on a Bruker NMR 500 DRX spectrometer. ^1H NMR spectra were referenced to the proton resonance resulting from incomplete deuteration of DMSO-d_6 (δ = 2.50) or $CDCl_3$ (δ = 7.26). The following abbreviations are used hereafter: s, singlet; d, doublet; t, triplet; q, quartet; and m, multiplet.

Electron paramagnetic resonance spectroscopy

EPR spectra were recorded by a Bruker Elexsys 500 X-band EPR spectrometer at 77 K. Samples were dispersed in DMA before EPR tests.

Gas chromatography

Gaseous products were analysed by GC using an Agilent 7890B gas chromatogram equipped with a Carboxen 1010 PLOT fused silica capillary column, thermal conductivity (TCD) and flame ionization detectors (FID) with nitrogen and hydrogen carrier gases, respectively. Approximately 200 µl of each gaseous sample was injected for each measurement. CH_4, CO and O_2 were detected by FID, while H_2 was detected by TCD.

Gas chromatography–mass spectrometry

Gaseous products were analysed by GC using a Shimadzu GCMS-QP2010 SE equipped with RT-Msieve 5A capillary column. A 200 µl portion of each gaseous sample was injected for each measurement. All gases were detected by an MS detector.

Time-resolved fluorescent spectra

Time-resolved fluorescent spectra were recorded on an ISS ChronosBH lifetime fluorometer. The excitation was set at 405 nm and the emission was set at 550 nm.

Synthesis of TFA-free Hf-Ir

Hf-Ir was treated with trimethylsilyl trifluoromethanesulfonate (TMSOTf) to replace capping TFA according to the previously reported method[57]. The resulting Hf-Ir-OTf was dispersed in a mixture of H_2O and acetonitrile (v:v = 1:9) to form a 1 mM dispersion (based on Ir-PS). Two equivalents of triethylamine (2 mM) was added to neutralize the generated triflic acid (HOTf). The solution was stirred at room temperature for 24 h. TFA-free Hf-Ir was separated by centrifugation and washed with acetonitrile twice.

MOZs for photocatalytic CO_2RR

To separate 4.6 ml vials were added 1 ml DMA, 11.2 mg BIH (50 mM, sacrificial reductant), 7.3 µl TFE (100 mM, proton source) and each modified MOZ (0.1 µM based on haemin and 1.25 µM based on Ir-PS). Each vial was sealed with a septum and degassed with CO_2 for 10 min before being stirred under visible-light irradiation (300 W Xenon lamp with 300 nm cutoff) at room temperature for 6 hours. A portion of 200 µl of gaseous products from each vial was collected in gas-tight syringes for GC analysis. Time-dependent photocatalytic CO_2RR of **MOZ-1**, **MOZ-2**, **MOZ-3** and **MOZ-4** were performed under the same conditions, while the gaseous products from each vial were continuously collected at 3 h, 6 h, 12 h, 24 h, 48 h and 72 h. All experiments were performed in triplicate.

Selectivity of CO_2RR

CH_4, CO and H_2 were the only products detected in this work. Selectivity for CO_2RR is therefore defined as:

$$\text{Selectivity} = \frac{\text{Number of CO} \times 2 + \text{Number of CH}_4 \times 8}{\text{Number of CO} \times 2 + \text{Number of CH}_4 \times 8 + \text{Number of H}_2 \times 2} \quad (1)$$

Quantum yield calculation

The quantum yields (QY) for the CO_2RR products were determined by the following equation:

$$QY_{CO_2RR} = \frac{\text{Number of generated CO} \times 2 + \text{Number of generated CH}_4 \times 8}{\text{Numbers of incident photons}} \quad (2)$$

The quantum yields for the WOR products were determined by the following equation:

$$QY_{WOR} = \frac{\text{Number of generated O}_2\text{ molecules} \times 4}{\text{Numbers of incident photons}} \quad (3)$$

The quantum yields for the artificial photosynthesis products were determined by the following equation:

$$QY_{total} = \frac{\text{Number of generated CO} \times 2 + \text{Number of generated CH}_4 \times 8}{\text{Numbers of incident photons/2}} \quad (4)$$

The number of incident photons was measured using $K_3Fe(C_2O_4)_3$ as chemical actinometer irradiated with a xenon lamp or sunlight with 350 ± 10 nm band-pass optical filter according to the literature[58] and known parameters[59]. The number of generated CO and CH_4 or O_2 was also measured under the same irradiation conditions (xenon lamp or sunlight with 350 ± 10 nm band-pass optical filter).

Stability of MOZs

The stability of MOZs was studied through a combination of powder X-ray diffraction and ICP-MS. Powder X-ray diffraction of MOZs recovered after reactions revealed the same pattern as freshly prepared MOZs (Supplementary Fig. 20e). ICP-MS analysis determined the leaching into the supernatant after reactions of <1% for Hf, <2% for Ir and <2% for Fe. Furthermore, the TONs of MOZ-catalysed CO_2RR showed a linear increase over time, indicating the stability of these MOZs in photocatalytic CO_2RR.

MOZs for sunlight-driven CO_2RR

To separate 4.6 ml vials were added 1 ml DMA, 11.2 mg BIH and 7.3 µl TFE. **MOZ-2**, **MOZ-3** or **MOZ-4** (0.1 µM based on haemin and 1.25 µM based on Ir-PS) was added to each vial, which was then sealed with a septum and degassed with CO_2 for 10 min before being stirred under direct natural sunlight at room temperature from 10:00 to 16:00 between 29 February and 4 March 2020 in Chicago, Illinois. A portion of 200 µl of gaseous products from each vial was collected on each day in gas-tight syringes for GC analysis.

MOZs for photocatalytic WOR

To separate 4.6 ml vials were added 0.5 ml acetonitrile (MeCN), 0.5 ml H_2O, 27 mg $K_2S_2O_8$ (100 mM, sacrificial oxidant) and each AA-modified MOZ (3.6 µM based on MBA-Ir and 45 µM based on Ir-PS). Each vial was sealed with a septum and degassed with N_2 for 10 min before being stirred under visible-light irradiation (300 W xenon lamp with 300 nm cutoff) at room temperature for 6 hours. A 200 µl portion of gaseous products from each vial was collected in gas-tight syringes for GC analysis. Time-dependent photocatalytic WOR of **MOZ-5**, **MOZ-6** and **MOZ-7** was performed under the same conditions, while the gaseous products from each vial were continuously collected at 3 h, 6 h, 12 h, 24 h, 48 h and 72 h. All experiments were performed in triplicate.

MOZs for total photocatalytic CO_2RR

To separate 23 ml vials were added 4 ml DMA, 1 ml H_2O, 90 µg $Co(bpy)_3Cl_2$ (30 µM), 36 µl TFE (100 mM), **MOZ-4** (0.3 µM based on haemin and 3.75 µM based on Ir-PS) and **MOZ-7** (0.9 µM based on MBA-Ir and 11.25 µM based on Ir-PS) or a homogeneous control (0.3 µM haemin, 0.9 µM Me-MBA-Ir and 15 µM Ir-PS). Each vial was sealed with a septum and degassed with CO_2 for 20 min before being stirred under visible-light irradiation for 3 h, 6 h, 12 h, 24 h and 48 h. A 200 µl of gaseous products from each vial was collected at each time point in gas-tight syringes for GC analysis. All experiments were performed in triplicate.

Data availability

Data relating to the characterization data of materials, detection of products, mechanistic studies, computational studies and NMR spectra are available in the Supplementary Information. Crystallographic data for the structures reported in this article have been deposited at the Cambridge Crystallographic Data Centre, under deposition numbers CCDC 2000080 (Ur). Copies of the data can be obtained free of charge via https://www.ccdc.cam.ac.uk/structures/. Cartesian coordinates of optimized structures are available in Supplementary Data 1. All additional data are available from the authors upon reasonable request.

References

1. Lee, D.-S., Nioche, P., Hamberg, M. & Raman, C. S. Structural insights into the evolutionary paths of oxylipin biosynthetic enzymes. *Nature* **455**, 363–368 (2008).
2. Berggren, G. et al. Biomimetic assembly and activation of [FeFe]-hydrogenases. *Nature* **499**, 66–69 (2013).
3. Helm, M. L., Stewart, M. P., Bullock, R. M., DuBois, M. R. & DuBois, D. L. A synthetic nickel electrocatalyst with a turnover frequency above 100,000 s^{-1} for H_2 production. *Science* **333**, 863–866 (2011).
4. Camara, J. M. & Rauchfuss, T. B. Combining acid–base, redox and substrate binding functionalities to give a complete model for the [FeFe]-hydrogenase. *Nat. Chem.* **4**, 26–30 (2012).
5. Ott, S., Kritikos, M., Åkermark, B., Sun, L. & Lomoth, R. A biomimetic pathway for hydrogen evolution from a model of the iron hydrogenase active site. *Angew. Chem. Int. Ed. Engl.* **43**, 1006–1009 (2004).
6. Wu, J. et al. Nanomaterials with enzyme-like characteristics (nanozymes): next-generation artificial enzymes (II). *Chem. Soc. Rev.* **48**, 1004–1076 (2019).
7. Takezawa, H., Shitozawa, K. & Fujita, M. Enhanced reactivity of twisted amides inside a molecular cage. *Nat. Chem.* **12**, 574–578 (2020).
8. Rabone, J. et al. An adaptable peptide-based porous material. *Science* **329**, 1053–1057 (2010).
9. Deng, H. et al. Large-pore apertures in a series of metal–organic frameworks. *Science* **336**, 1018–1023 (2012).
10. Xiao, D. J. et al. Oxidation of ethane to ethanol by N_2O in a metal–organic framework with coordinatively unsaturated iron(II) sites. *Nat. Chem.* **6**, 590–595 (2014).
11. Nath, I., Chakraborty, J. & Verpoort, F. Metal organic frameworks mimicking natural enzymes: a structural and functional analogy. *Chem. Soc. Rev.* **45**, 4127–4170 (2016).
12. Furukawa, H., Cordova Kyle, E., O'Keeffe, M. & Yaghi Omar, M. The chemistry and applications of metal–organic frameworks. *Science* **341**, 1230444 (2013).
13. Li, L. et al. Ethane/ethylene separation in a metal–organic framework with iron-peroxo sites. *Science* **362**, 443–446 (2018).
14. Ji, S. et al. Matching the kinetics of natural enzymes with a single-atom iron nanozyme. *Nat. Catal.* **4**, 407–417 (2021).
15. Scott, S., Zhao, H., Dey, A. & Gunnoe, T. B. Nano-apples and orange-zymes. *ACS Catal.* **10**, 14315–14317 (2020).

16. Dai, R. et al. Electron crystallography reveals atomic structures of metal–organic nanoplates with $M_{12}(\mu_3\text{-}O)_8(\mu_3\text{-}OH)_8(\mu_2\text{-}OH)_6$ (M=Zr, Hf) secondary building units. *Inorg. Chem.* **56**, 8128–8134 (2017).
17. Rao, H., Schmidt, L. C., Bonin, J. & Robert, M. Visible-light-driven methane formation from CO_2 with a molecular iron catalyst. *Nature* **548**, 74–77 (2017).
18. Mariano, R. G., McKelvey, K., White, H. S. & Kanan, M. W. Selective increase in CO_2 electroreduction activity at grain–boundary surface terminations. *Science* **358**, 1187–1192 (2017).
19. García de Arquer, F. P. et al. CO_2 electrolysis to multicarbon products at activities greater than 1 A cm^{-2}. *Science* **367**, 661–666 (2020).
20. Morales-Guio, C. G. et al. Improved CO_2 reduction activity towards C_{2+} alcohols on a tandem gold on copper electrocatalyst. *Nat. Catal.* **1**, 764–771 (2018).
21. Liu, C., Colón, B. C., Ziesack, M., Silver, P. A. & Nocera, D. G. Water splitting–biosynthetic system with CO_2 reduction efficiencies exceeding photosynthesis. *Science* **352**, 1210–1213 (2016).
22. Smith, P. T., Kim, Y., Benke, B. P., Kim, K. & Chang, C. J. Supramolecular tuning enables selective oxygen reduction catalyzed by cobalt porphyrins for direct electrosynthesis of hydrogen peroxide. *Angew. Chem. Int. Ed. Engl.* **59**, 4902–4907 (2020).
23. Ju, W. et al. Unraveling mechanistic reaction pathways of the electrochemical CO_2 reduction on Fe–N–C single-site catalysts. *ACS Energy Lett.* **4**, 1663–1671 (2019).
24. Rao, H., Lim, C.-H., Bonin, J., Miyake, G. M. & Robert, M. Visible-light-driven conversion of CO_2 to CH_4 with an organic sensitizer and an iron porphyrin catalyst. *J. Am. Chem. Soc.* **140**, 17830–17834 (2018).
25. Costentin, C., Drouet, S., Passard, G., Robert, M. & Savéant, J.-M. Proton-coupled electron transfer cleavage of heavy-atom bonds in electrocatalytic processes. Cleavage of a C–O bond in the catalyzed electrochemical reduction of CO_2. *J. Am. Chem. Soc.* **135**, 9023–9031 (2013).
26. Gotico, P. et al. Second-sphere biomimetic multipoint hydrogen-bonding patterns to boost CO_2 reduction of iron porphyrins. *Angew. Chem. Int. Ed. Engl.* **58**, 4504–4509 (2019).
27. Davethu, P. A. & de Visser, S. P. CO_2 reduction on an iron-porphyrin center: a computational study. *J. Phy. Chem. A* **123**, 6527–6535 (2019).
28. Zhai, Q. et al. Photocatalytic conversion of carbon dioxide with water into methane: platinum and copper(I) oxide co-catalysts with a core–shell structure. *Angew. Chem. Int. Ed. Engl.* **52**, 5776–5779 (2013).
29. Xie, S., Wang, Y., Zhang, Q., Deng, W. & Wang, Y. MgO- and Pt-promoted TiO_2 as an efficient photocatalyst for the preferential reduction of carbon dioxide in the presence of water. *ACS Catal.* **4**, 3644–3653 (2014).
30. Wang, Y. et al. High efficiency photocatalytic conversion of CO_2 with H_2O over Pt/TiO_2 nanoparticles. *RSC Adv.* **4**, 44442–44451 (2014).
31. Long, R. et al. Isolation of Cu atoms in Pd lattice: forming highly selective sites for photocatalytic conversion of CO_2 to CH_4. *J. Am. Chem. Soc.* **139**, 4486–4492 (2017).
32. Li, R. et al. Integration of an inorganic semiconductor with a metal–organic framework: a platform for enhanced gaseous photocatalytic reactions. *Adv. Mater.* **26**, 4783–4788 (2014).
33. Duan, L. et al. A molecular ruthenium catalyst with water-oxidation activity comparable to that of photosystem II. *Nat. Chem.* **4**, 418–423 (2012).
34. Wang, C., Wang, J.-L. & Lin, W. Elucidating molecular iridium water oxidation catalysts using metal–organic frameworks: a comprehensive structural, catalytic, spectroscopic, and kinetic study. *J. Am. Chem. Soc.* **134**, 19895–19908 (2012).
35. Duan, L., Xu, Y., Zhang, P., Wang, M. & Sun, L. Visible light-driven water oxidation by a molecular ruthenium catalyst in homogeneous system. *Inorg. Chem.* **49**, 209–215 (2010).
36. Han, J. et al. Metal–organic framework immobilized cobalt oxide nanoparticles for efficient photocatalytic water oxidation. *J. Mater. Chem. A* **3**, 20607–20613 (2015).
37. Maeda, K. et al. Photocatalyst releasing hydrogen from water. *Nature* **440**, 295–295 (2006).
38. Wang, Q. et al. Oxysulfide photocatalyst for visible-light-driven overall water splitting. *Nat. Mater.* **18**, 827–832 (2019).
39. Kumar, A. et al. Biochar-templated $g\text{-}C_3N_4/Bi_2O_2CO_3/CoFe_2O_4$ nano-assembly for visible and solar assisted photo-degradation of paraquat, nitrophenol reduction and CO_2 conversion. *Chem. Eng. J.* **339**, 393–410 (2018).
40. Jiang, Z. et al. A hierarchical Z-scheme $\alpha\text{-}Fe_2O_3/g\text{-}C_3N_4$ hybrid for enhanced photocatalytic CO_2 reduction. *Adv. Mater.* **30**, 1706108 (2018).
41. Wang, J. et al. Exceptional photocatalytic activities for CO_2 conversion on AlO bridged $g\text{-}C_3N_4/\alpha\text{-}Fe_2O_3$ z-scheme nanocomposites and mechanism insight with isotopesZ. *Appl. Catal. B* **221**, 459–466 (2018).
42. Bae, K.-L., Kim, J., Lim, C. K., Nam, K. M. & Song, H. Colloidal zinc oxide-copper(I) oxide nanocatalysts for selective aqueous photocatalytic carbon dioxide conversion into methane. *Nat. Commun.* **8**, 1156 (2017).
43. Jin, J., Yu, J., Guo, D., Cui, C. & Ho, W. A hierarchical Z-scheme CdS–WO_3 photocatalyst with enhanced CO_2 reduction activity. *Small* **11**, 5262–5271 (2015).
44. Aguirre, M. E., Zhou, R., Eugene, A. J., Guzman, M. I. & Grela, M. A. Cu_2O/TiO_2 heterostructures for CO_2 reduction through a direct Z-scheme: protecting Cu_2O from photocorrosion. *Appl. Catal. B* **217**, 485–493 (2017).
45. Shen, Y. et al. Artificial trees for artificial photosynthesis: construction of dendrite-structured $\alpha\text{-}Fe_2O_3/g\text{-}C_3N_4$ Z-scheme system for efficient CO_2 reduction into solar fuels. *ACS Appl. Energy Mater.* **3**, 6561–6572 (2020).
46. Han, Q. et al. Elegant construction of $ZnIn_2S_4/BiVO_4$ hierarchical heterostructures as direct Z-scheme photocatalysts for efficient CO_2 photoreduction. *ACS Appl. Mater. Interfaces* **13**, 15092–15100 (2021).
47. Guo, R.-t et al. Photocatalytic reduction of CO_2 into CO over nanostructure Bi_2S_3 quantum dots/$g\text{-}C_3N_4$ composites with Z-scheme mechanism. *Appl. Surf. Sci.* **500**, 144059 (2020).
48. Jiang, Z. et al. Filling metal–organic framework mesopores with TiO_2 for CO_2 photoreduction. *Nature* **586**, 549–554 (2020).
49. Liang, L. et al. Infrared light-driven CO_2 overall splitting at room temperature. *Joule* **2**, 1004–1016 (2018).
50. Wu, L.-Y. et al. Encapsulating perovskite quantum dots in iron-based metal–organic frameworks (MOFs) for efficient photocatalytic CO_2 reduction. *Angew. Chem. Int. Ed. Engl.* **58**, 9491–9495 (2019).
51. Zhu, Y.-Y. et al. Merging photoredox and organometallic catalysts in a metal–organic framework significantly boosts photocatalytic activities. *Angew. Chem. Int. Ed. Engl.* **57**, 14090–14094 (2018).
52. Zhu, X.-Q., Zhang, M.-T., Yu, A., Wang, C.-H. & Cheng, J.-P. Hydride, hydrogen atom, proton, and electron transfer driving forces of various five-membered heterocyclic organic hydrides and their reaction intermediates in acetonitrile. *J. Am. Chem. Soc.* **130**, 2501–2516 (2008).
53. Maeda, K. Z-Scheme water splitting using two different semiconductor photocatalysts. *ACS Catal.* **3**, 1486–1503 (2013).
54. Sheldrick, G. M. Crystal structure refinement with SHELXL. *Acta Crystallogr. C* **71**, 3–8 (2015).

55. Dolomanov, O. V., Bourhis, L. J., Gildea, R. J., Howard, J. A. & Puschmann, H. OLEX2: a complete structure solution, refinement and analysis program. *J. Appl. Crystallogr.* **42**, 339–341 (2009).
56. Sheldrick, G. M. A short history of SHELX. *Acta Crystallogr. A* **64**, 112–122 (2008).
57. Quan, Y. et al. Metal–organic layers for synergistic Lewis acid and photoredox catalysis. *J. Am. Chem. Soc.* **142**, 1746–1751 (2020).
58. Chen, X. et al. Ultrathin, single-crystal WO_3 nanosheets by two-dimensional oriented attachment toward enhanced photocatalystic reduction of CO_2 into hydrocarbon fuels under visible light. *ACS Appl. Mater. Interfaces* **4**, 3372–3377 (2012).
59. Lide, D. R. *CRC Handbook of Chemistry and Physics* Vol. 85 (CRC Press, 2004).

Acknowledgements

We thank F. Shi for help with scanning transmission electron microscopy. This work made use of Instruments in the Electron Microscopy Core (Research Resources Center, University of Illinois at Chicago). We thank G. Zhang, X. Jiang, C. Wang and F. Shi for helpful discussions. This work was supported by the University of Chicago and National Science Foundation (CHE-2102554). W.S. acknowledges financial support from the China Scholarship Council. Single-crystal diffraction studies were performed at ChemMatCARS, APS, ANL. ChemMatCARS is principally supported by the Divisions of Chemistry (CHE) and Materials Research (DMR), National Science Foundation, under grant NSF/CHE-1346572. Use of the Advanced Photon Source, an Office of Science User Facility operated for the US Department of Energy (DOE) Office of Science by Argonne National Laboratory, was supported by the US DOE under contract DE-AC02-06CH11357.

Author contributions

G.L., Y.F., W.S., S.S.V. and W.L. conceived the idea and designed the project. W.L. directed and supervised the research. G.L., Y.F. and E.Y. performed the experimental works. W.S. performed the computational works. G.L., Y.F., W.S., S.S.V. and W.L. wrote the paper, with input from all other co-authors.

Competing interests

The authors declare no competing interests.

Additional information

Supplementary information The online version contains supplementary material available at https://doi.org/10.1038/s41929-022-00865-5.

Correspondence and requests for materials should be addressed to Wenbin Lin.

Peer review information *Nature Catalysis* thanks Jun Cheng and the other, anonymous, reviewer(s) for their contribution to the peer review of this work.